Fast and Reliable Reconstruction of 3-D Arbitrary Anisotropic Objects Buried in Layered Media by Cascaded Inverse Solvers

Xianliang Huang, Jiawen Li, Jianliang Zhuo, Feng Han, *Senior Member, IEEE*, and Qing Huo Liu, *Fellow, IEEE*

***Abstract*— In this letter, a new full-wave inversion (FWI) scheme is proposed to reconstruct multiple dielectric parameters of 3-D arbitrary anisotropic objects buried in layered media. Three inverse solvers, including the isotropic one, biaxial anisotropic one, and the arbitrary anisotropic one, are cascaded sequentially. The dielectric parameters obtained by the first solver are used as the initial values of the next solver. Meanwhile, the inversion domain is synchronously downsized on the basis of discrepancies between the inverted dielectric parameters and the background ones. Numerical simulations show that, compared with the direct arbitrary anisotropic inverse solver, the cascading inversion scheme not only can produce more reliable reconstructed profiles but also significantly lowers the computational cost. In addition, the antinoise ability of the cascaded solvers is also tested.**

***Index Terms*— Arbitrary anisotropy, cascaded inverse solvers, full-wave inversion (FWI).**

I. Introduction

ELECTROMAGNETIC (EM) inverse scattering is to reconstruct shapes, positions, dielectric parameters, and others of unknown objects located in a region of interest from the measured EM data. It has wide applications in geophysical exploration [1], biomedical imaging [2], through-wall imaging [3], and so on.

The inverse scattering methods can be roughly categorized into the model-based inversion and the voxel-based inversion according to the availability of *a priori* information [4]. Compared with the model-based inversion, the voxel-based inversion requires the inversion domain to be discretized. This often generates a huge number of unknowns in 3-D inversion problems and results in severe ill-posedness. However, its advantage is that the model parameters of scatterers are allowed to have arbitrary spatial distribution in the inversion domain. Meanwhile, no *a priori* information is required. Therefore, the voxel-based inversion has intensively attracted the attention of researchers in the past decades, and several full-wave inversion (FWI) methods have been proposed. For example, the Born iterative method (BIM) iteratively solves the state equation in the forward scattering and the data equation in the inverse scattering [5]. The total field in the current iteration is replaced by that obtained in the last iteration to linearize the data equation. The distorted BIM (DBIM) [6] and variational BIM (VBIM) [7] are the variants of BIM and also have wide applications. Different from BIM, the contrast source inversion (CSI) has no forward computation and the cost function is constructed using the summation of mismatches in the data equation and the state equation. The subspace-based optimization method (SOM) [8] is implemented similar to CSI but for a subspace of the induced current.

In most previous works related to 3-D EM FWI, the aforementioned methods are applied to the reconstruction of isotropic objects. However, 3-D anisotropy is common in engineering applications, e.g., geophysical prospecting [9] and composite material imaging [10]. Unfortunately, because multiple dielectric parameters in a single discretized cell are reconstructed simultaneously in the 3-D voxel-based anisotropic inversion, the underdetermination becomes quite severe. In this work, we mitigate the underdetermination for the inversion of arbitrary anisotropic objects by cascading three inverse solvers and downsizing the inversion domain step by step. First, the isotropic inverse solver reconstructs the approximate isotropic dielectric parameters. These isotropic values will be used as the initial values of the biaxial anisotropic inverse solver. Meanwhile, the inversion domain is downsized by measuring the discrepancies between the reconstructed parameters and the corresponding background parameters with a threshold. Then, a similar process will also be used to bridge the biaxial anisotropic inverse solver and the arbitrary anisotropic one and to further compress the inversion domain. As a consequence, the unknowns of the discretized data equation decrease, the convergence of the iteration becomes faster, and the solution is more accurate.

The organization of this letter is as follows. In Section II, the 3-D EM forward and inversion models for FWI are briefly formulated. Then, the cascading scheme for three types of inverse solvers is described in detail. In Section III, a numerical example is used to verify the superiority of the proposed scheme. Finally, in Section IV, the conclusion is drawn.

Manuscript received January 16, 2021; revised April 3, 2021; accepted April 26, 2021. Date of publication May 11, 2021; date of current version January 5, 2022. This work was supported by the National Key Research and Development Program of the Ministry of Science and Technology of China under Grant 2018YFF01013300 and Grant 2018YFC0603503. *(Corresponding authors: Feng Han; Qing Huo Liu.)*

Xianliang Huang, Jiawen Li, Jianliang Zhuo, and Feng Han are with the Key Laboratory of Electromagnetic Wave Science and Detection Technology, Institute of Electromagnetics and Acoustics, Xiamen University, Xiamen 361005, China (e-mail: feng.han@xmu.edu.cn).

Qing Huo Liu is with the Department of Electrical and Computer Engineering, Duke University, Durham, NC 27708 USA (e-mail: qhliu@duke.edu).

Digital Object Identifier 10.1109/LGRS.2021.3076433

II. Theory and Methods

A. Forward and Inversion Models

The forward scattering of 3-D objects with arbitrary anisotropy embedded in layered media is formulated by the electric field integral equation (EFIE)

$$\mathbf{E}_{\text{inc}}(\mathbf{r}) = \mathbf{E}_{\text{tot}}(\mathbf{r}) - j\omega\varepsilon_0 \int_D \overline{\overline{\mathbf{G}}}_{\mathbf{EJ}}(\mathbf{r},\mathbf{r}')\left[\overline{\overline{\epsilon}}_s(\mathbf{r}') - \overline{\overline{\epsilon}}_b(\mathbf{r}')\right]\mathbf{E}_{\text{tot}}(\mathbf{r}')d\mathbf{r}' \quad (1)$$

where $\mathbf{E}_{\text{inc}}$ is the incident field in the inversion domain D when the anisotropic scatterer is absent and $\mathbf{E}_{\text{tot}}$ is the total field when the scatterer is present. $\overline{\overline{\mathbf{G}}}_{\mathbf{EJ}}$ is the dyadic Green's function (DGF) in layered media [11] linking the source point $\mathbf{r}'$ and the field point $\mathbf{r}$. $\overline{\overline{\epsilon}}_s$ and $\overline{\overline{\epsilon}}_b$ are the relative complex permittivity of the scatterer and the background medium, respectively. Their detailed expressions can be found in [12] and [13]. The inversion model is formulated by the data equations

$$\mathbf{E}_{\text{sct}}(\mathbf{r}) = j\omega\varepsilon_0 \int_D \overline{\overline{\mathbf{G}}}_{\mathbf{EJ}}(\mathbf{r},\mathbf{r}')\left[\overline{\overline{\epsilon}}_s(\mathbf{r}') - \overline{\overline{\epsilon}}_b(\mathbf{r}')\right]\mathbf{E}_{\text{tot}}(\mathbf{r}')d\mathbf{r}' \quad (2a)$$

$$\mathbf{H}_{\text{sct}}(\mathbf{r}) = j\omega\varepsilon_0 \int_D \overline{\overline{\mathbf{G}}}_{\mathbf{HJ}}(\mathbf{r},\mathbf{r}')\left[\overline{\overline{\epsilon}}_s(\mathbf{r}') - \overline{\overline{\epsilon}}_b(\mathbf{r}')\right]\mathbf{E}_{\text{tot}}(\mathbf{r}')d\mathbf{r}' \quad (2b)$$

where $\mathbf{E}_{\text{sct}}$ and $\mathbf{H}_{\text{sct}}$ are the scattered electric field and magnetic field measured at the receiver array, respectively. In the forward computation, (1) is discretized and $\mathbf{E}_{\text{tot}}$ is solved by the stabilized biconjugate-gradient fast Fourier transform (BCGS-FFT). In the inversion, (2) is discretized and VBIM is adopted to solve $\overline{\overline{\epsilon}}_s$. This alternative iteration continues until the data misfit between the measured scattered field and that computed by (2) reaches a stop criterion. Details of BCGS-FFT and VBIM for arbitrary anisotropic scatterers can be found in [14]. One should note that (1) and (2) can easily degenerate into the formulas for the scattering and inverse scattering of biaxial anisotropic and isotropic objects. The implementation of BCGS-FFT and VBIM for biaxial and isotropic scatterers is given in [15] and [6]. In addition, we only consider the nonmagnetic scatterers, and $\overline{\overline{\epsilon}}_s$ of the arbitrary anisotropic scatterer is symmetrical [12]. Therefore, there are twelve unknowns (six for permittivity and six for conductivity) for arbitrary anisotropic scatterers, six unknowns (three for permittivity and three for conductivity) for biaxial scatterers, and two unknowns (one for permittivity and one for conductivity) for isotropic scatterers to reconstruct.

B. Cascading Scheme of Three Inverse Solvers

Direct inversion of 12 unknowns of arbitrary anisotropic scatterers by VBIM is challenging due to the strong ill-posedness of inverse scattering problems [14]. Therefore, we first use the isotropic inverse solver to find the approximate model parameters, e.g., isotropic permittivity and conductivity, of the arbitrary anisotropic scatterers. Because there are only two model parameters to reconstruct in each discretized cell, the ill-posedness is significantly alleviated. Then, we judge the kth discretized cell as "background" by using

$$\frac{|\xi_i^k - \xi_b|}{|\xi_b|} \le \text{th} \quad (3)$$

and remove it from the inversion domain. ξ_i^k is the inverted model parameter in the kth cell and ξ_b is the background model parameter of the inversion domain. The parameter th is an empirical but small threshold value. Equation (3) means that a certain cell will be treated as "background" and removed if the reconstructed model parameter in that cell is approaching the background model parameter. The word "remove" means that the unknowns in the confirmed "background" cell will be discarded in the discretized data equations and the corresponding row vectors in the Fréchet derivative matrix in the inversion are deleted. In this way, the inversion domain is compressed and the computational cost is also lowered. In the next step, we use the reconstructed isotropic model parameters as initial values of the biaxial anisotropic inverse solver and implement the reconstruction in the downsized inversion domain. Although there are six model parameters to reconstruct in each discretized cell, the ill-posedness is not severe because the inversion domain has been compressed. Finally, the arbitrary anisotropic inversion is implemented following the similar procedure. Two points must be emphasized here: 1) if there are multiple dielectric parameters to reconstruct for a certain discretized cell, (3) must be satisfied for all the parameters simultaneously and 2) if ξ_b is zero for a certain dielectric parameter, it will not be used in (3) to judge the "background" cell.

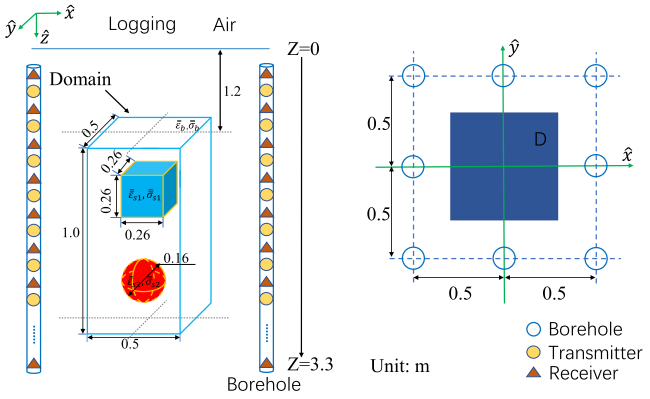

Fig. 1. Cross-well model. (Left) Illustration of the model and (Right) location sketch of the boreholes in the xy plane.

III. Numerical Results

In this section, we apply the proposed scheme to a cross-well model to reconstruct 12 anisotropic parameters simultaneously. The empirical threshold th in (3) is set as 0.1.

A. Model Configuration

As shown in Fig. 1, a cube and a sphere are buried in the well. The sizes of the inversion domain and two objects are labeled. Before rotation of the optical axes of two objects, the dielectric parameters of the cube are

$$\overline{\overline{\varepsilon}}_{s1} = \text{diag}\{2.5, 2.3, 2.6\}\ \overline{\overline{\sigma}}_{s1} = \text{diag}\{7, 8, 13\}\ \text{mS/m} \quad (4)$$

TABLE I
RELATIVE PERMITTIVITY AND CONDUCTIVITY OF THE CUBE AND SPHERE WITH ARBITRARY ANISOTROPY

	ε_{11}	ε_{12}	ε_{13}	ε_{22}	ε_{23}	ε_{33}	σ_{11}	σ_{12}	σ_{13}	σ_{22}	σ_{23}	σ_{33}
cube	2.487	-0.0216	0.075	2.462	0.1229	2.45	7.500	1.100	0.866	8.500	1.266	12.50
sphere	3.200	-0.0732	-0.050	3.00	-0.046	2.900	10.60	0.866	0.250	11.90	0.433	9.00

Remark: the unit of σ is mS/m.

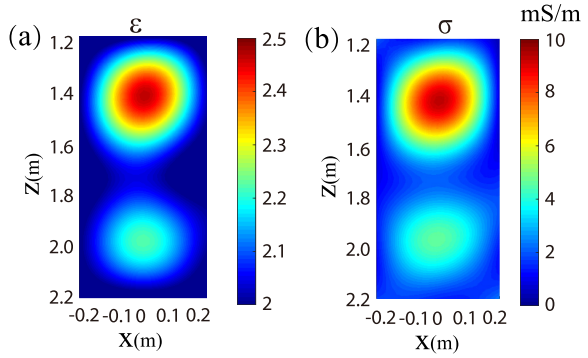

Fig. 2. Reconstructed isotropic profiles. (a) Permittivity. (b) Conductivity.

and those of the sphere are

$$\overline{\overline{\varepsilon}}_{s2} = \text{diag}\{3.3, 3.0, 2.8\}\ \overline{\overline{\sigma}}_{s2} = \text{diag}\{11, 12, 10\}\ \text{mS/m}. \quad (5)$$

The rotation angles of optical axes of both the cube and sphere are $\phi_1 = 30°$ and $\phi_2 = 45°$ (see [13, Fig. 2]). Their dielectric parameters after the rotation of optical axes are listed in Table I. In addition, one should note that the background medium is homogeneous with the parameter $\varepsilon_b = 2.0$ and $\sigma_b = 2.0$ mS/m. Seventeen receivers and sixteen transmitters are placed in each borehole. Eight boreholes are drilled around the inversion domain, and the locations are shown in the right part of Fig. 1. The operating frequency is 250 MHz. All the simulations are performed on a workstation with 20-core Xeon E2650 v3 2.3G CPU, 512-GB RAM. All the measured scattered field data are synthesized by the BCGS-FFT forward solver.

B. Comparison Between the Cascading Scheme and the Direct Inversion

We first employ the cascading scheme to reconstruct the arbitrary anisotropic objects. The inverted profiles by the isotropic inverse solver are shown in Fig. 2. We can see that the solver only finds the approximate locations of two objects. The reconstructed shape of the cube is close to a sphere. The inverted dielectric parameters of the sphere are far from the ground truth. Then, we apply (3) to the inversion results and remove partial "background" cells to downsize the inversion domain. In the second step, we treat the unknown objects as biaxial anisotropic ones and use the inversion results from the isotropic solver as the initial profiles and perform the VBIM inversion. The results are shown in Fig. 3. Compared with the profiles shown in Fig. 2, the retrieved permittivity and conductivity values of the sphere become larger, which are closer to the ground truth. Meanwhile, because partial "background" cells are removed, the boundary of the reconstructed

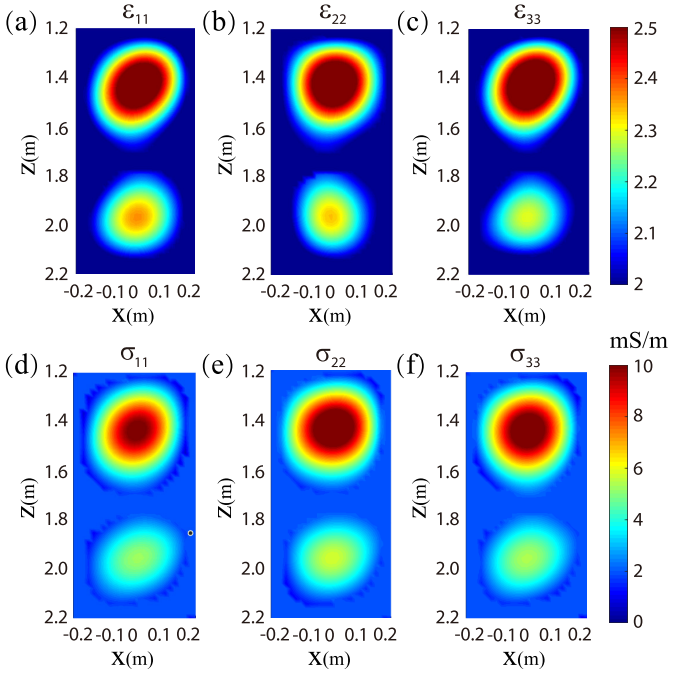

Fig. 3. Reconstructed biaxial anisotropic profiles. (a)–(c) Permittivities. (d)–(f) Conductivities.

cube becomes sharper. Then, in the final step, we remove partial "background" cells once more based on the results of the biaxial inverse solver and reconstruct 12 model parameters of the arbitrary anisotropic objects simultaneously. The results are shown in Fig. 4. We can see that the cubic shape of the cube clearly shows up. In addition, the dielectric parameters of both objects approach the ground truth.

Fig. 5 shows the reconstructed 12 dielectric parameters of the arbitrary anisotropic objects by using the direct VBIM inversion. By comparing with the inversion results shown in Fig. 4, we made three observations. First, the shape of the cube is not well reconstructed by the direct inversion. This is because the inversion domain is fixed in the direct inversion but is effectively downsized in the cascading scheme. As a result, the underdetermination of the inverse problem is severe for the direct inversion but is mitigated in the cascading scheme. Second, the dielectric parameters obtained by the direct inversion are less than the ground-truth values. Since the shapes of the objects are not constrained in the direct inversion, the reconstructed volumes of the objects are usually larger than their true volumes. Consequently, the values of the inverted model parameters become less than the true values. Finally, the quantitative fit between reconstructed profiles and true profiles is measured by the structural similarity (SSIM) index

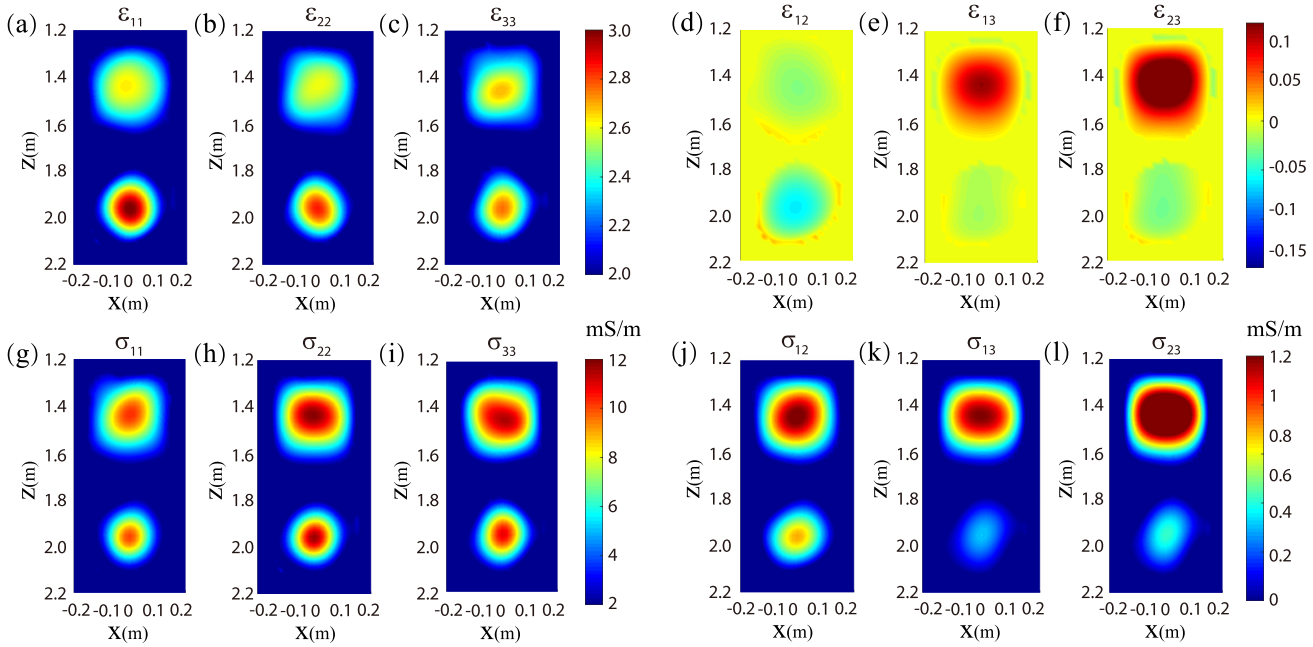

Fig. 4. Reconstructed arbitrary anisotropic profiles by the cascading scheme. (a)–(f) Permittivities. (g)–(l) Conductivities.

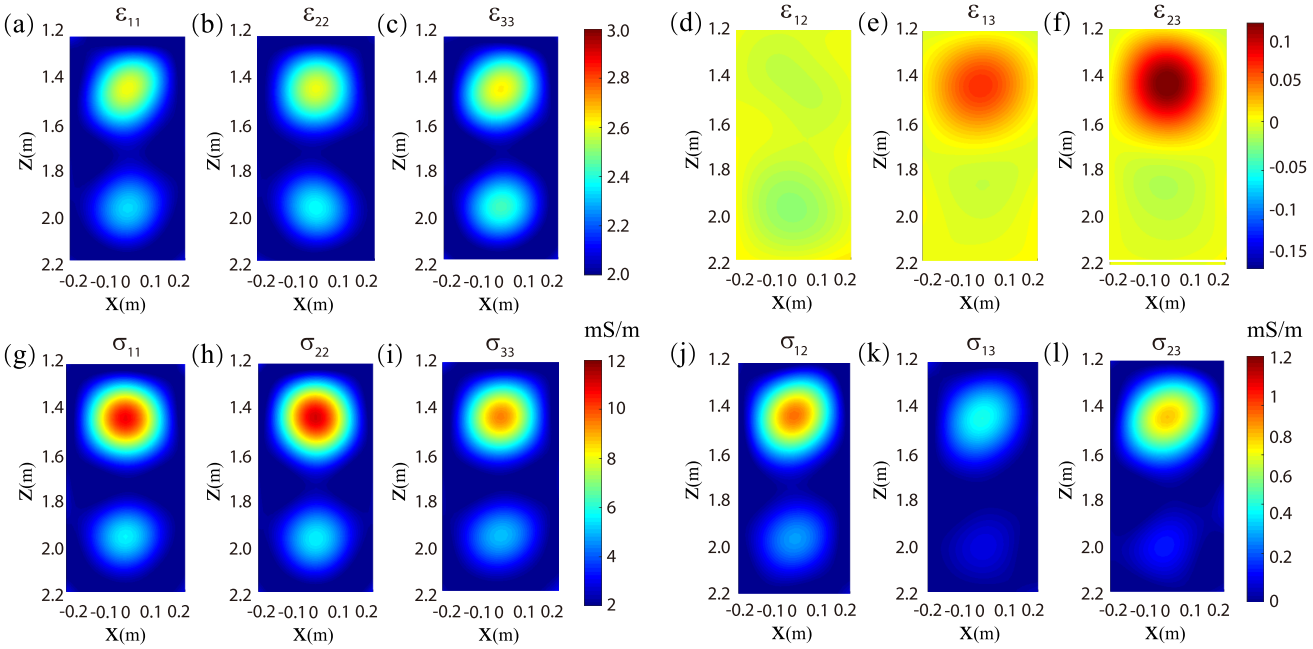

Fig. 5. Reconstructed arbitrary anisotropic profiles by the direct inversion. (a)–(f) Permittivities. (g)–(l) Conductivities.

TABLE II

SSIMs Between Reconstructed Parameters and Ground Truths Based on Two Inversion Methods

	ε_{11}	ε_{12}	ε_{13}	ε_{22}	ε_{23}	ε_{33}	σ_{11}	σ_{12}	σ_{13}	σ_{22}	σ_{23}	σ_{33}
cascading scheme	0.7556	0.7837	0.7578	0.7373	0.7712	0.7229	0.7388	0.7042	0.7254	0.7396	0.7547	0.7522
direct inversion	0.6590	0.6717	0.6488	0.6406	0.6728	0.5638	0.5868	0.5501	0.5488	0.5721	0.5992	0.5951

presented in [16]. The SSIM values for the cascading scheme are roughly 0.1 larger than those for the direct inversion. The details are listed in Table II.

Fig. 6 shows the comparisons of typical 3-D isosurfaces of the reconstructed profiles. The cubic shapes are clearly displayed for the inversion by the cascading scheme. Another observation is that the volume of the sphere in the isosurface plots is smaller for the direct inversion than that for the inversion by the cascading scheme. This is because the reconstructed dielectric parameter values are smaller in the

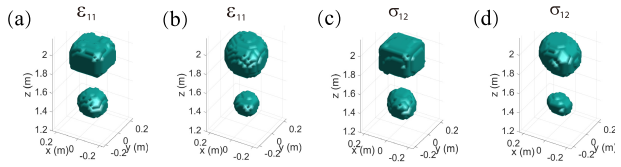

Fig. 6. 3-D isosurface plots of typical reconstructed dielectric parameters. (a) ε_{11} by the cascading scheme. (b) ε_{11} by the direct inversion. (c) σ_{12} by the cascading scheme. (d) σ_{12} by the direct inversion. The isovalue is 2.2 for ε_{11} and 0.3 mS/m for σ_{12}.

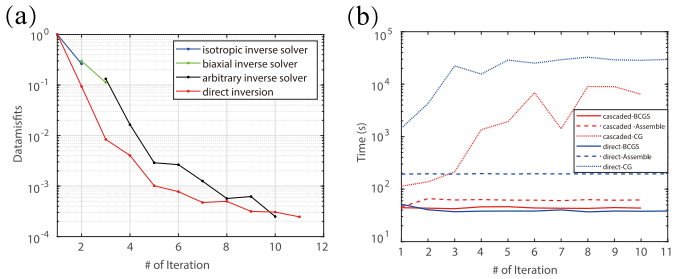

Fig. 7. Comparison of the cascading scheme and the direct inversion in different iteration steps. (a) Convergence curves. (b) Computational time for BCGS-FFT and assembling the matrix and CG in VBIM.

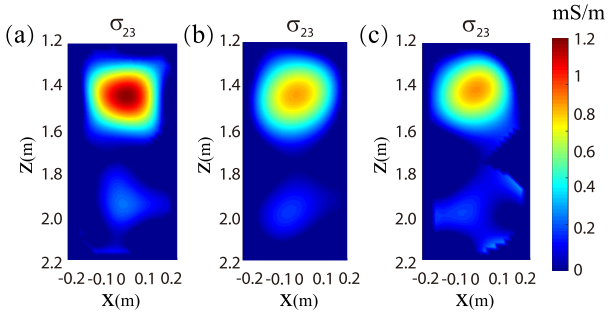

Fig. 8. 2-D slices at $y = 0$ of the reconstructed σ_{23} for different noise levels. (a) 30 dB. (b) 20 dB. (c) 10 dB.

direct inversion. Fig. 7(a) shows the convergence curves of the cascading scheme and the direct inversion. We can see that there is no big difference between the two methods. However, the computational cost is obviously different, as is shown in Fig. 7(b). Because the inversion domain is compressed in the cascading scheme, the computational time for assembling the Fréchet derivative matrix and the conjugate gradient (CG) in the VBIM [14] is significantly lowered. However, the forward computation time has no obvious difference for the two schemes since the computation domain remains the same in all iterations for the forward BCGS solver.

C. Antinoise Test

We then test the inversion performance of the proposed cascading scheme when 30-, 20-, and 10-dB noises are used to contaminate the measured fields. Here, the noise level is defined according to the signal-to-noise ratio (SNR) of power. Due to space limitation, only the 2-D slices of the reconstructed σ_{23} profiles for different noise levels are shown in Fig. 8. We can see that the cascading scheme shows good robustness to noise. Even when the 10-dB noise is added, two reconstructed objects are discernible although the shapes are distorted and the values deviate away from the ground truth.

IV. Conclusion

In this work, three inverse solvers are sequentially cascaded together to reconstruct the 3-D arbitrary anisotropic objects. The computational cost is lowered because the inversion domain is downsized for the biaxial anisotropic inverse solver and the arbitrary anisotropic one. The reconstruction accuracy is enhanced since the ill-posedness of the inversion is effectively alleviated. In addition, the antinoise ability of the proposed cascading scheme is also justified. The future work will focus on the inversion of field measured data based on the cascading scheme.

References

[1] G. L. Wang, T. Barber, P. Wu, D. Allen, and A. Abubakar, "Fast inversion of triaxial induction data in dipping crossbedded formations," *Geophysics*, vol. 82, no. 2, pp. D31–D45, Mar. 2017.

[2] S. Y. Semenov *et al.*, "Microwave tomography: Two-dimensional system for biological imaging," *IEEE Trans. Biomed. Eng.*, vol. 43, no. 9, pp. 869–877, Sep. 1996.

[3] T. Lu, K. Agarwal, Y. Zhong, and X. Chen, "Through-wall imaging: Application of subspace-based optimization method," *IEEE Prog. Electromagn. Res.*, vol. 102, pp. 351–366, 2010.

[4] M. Li, A. Abubakar, and T. M. Habashy, "A three-dimensional model-based inversion algorithm using radial basis functions for microwave data," *IEEE Trans. Antennas Propag.*, vol. 60, no. 7, pp. 3361–3372, Jul. 2012.

[5] Y. Zhong, M. Lambert, D. Lesselier, and X. Chen, "A new integral equation method to solve highly nonlinear inverse scattering problems," *IEEE Trans. Antennas Propag.*, vol. 64, no. 5, pp. 1788–1798, May 2016.

[6] F. Li, Q. H. Liu, and L.-P. Song, "Three-dimensional reconstruction of objects buried in layered media using Born and distorted Born iterative methods," *IEEE Geosci. Remote Sens. Lett.*, vol. 1, no. 2, pp. 107–111, Apr. 2004.

[7] N. Zaiping, Y. Feng, Z. Yanwen, and Z. Yerong, "Variational Born iteration method and its applications to hybrid inversion," *IEEE Trans. Geosci. Remote Sens.*, vol. 38, no. 4, pp. 1709–1715, Jul. 2000.

[8] X. Chen, "Subspace-based optimization method for solving inverse-scattering problems," *IEEE Trans. Geosci. Remote Sens.*, vol. 48, no. 1, pp. 42–49, Jan. 2010.

[9] O. V. Pankratov, A. V. Kuvshinov, and D. B. Avdeev, "High-performance three-dimensional electromagnetic modelling using modified Neumann series. Anisotropic Earth," *J. Geomagn. Geoelectr.*, vol. 49, no. 11, pp. 1541–1547, 1997.

[10] D. Lesselier, P.-P. Ding, G. Rodeghiero, M. Lambert, and Y. Zhong, "On inverse scattering and imaging solutions for objects buried within uniaxially anisotropic media," in *Proc. IEEE 15th Medit. Microw. Symp. (MMS)*, Nov. 2015, pp. 1–4.

[11] K. A. Michalski and J. R. Mosig, "Multilayered media Green's functions in integral equation formulations," *IEEE Trans. Antennas Propag.*, vol. 45, no. 3, pp. 508–519, Mar. 1997.

[12] J. Wang, J. Li, Y. Chen, F. Han, and Q. H. Liu, "Simulation of 3-D electromagnetic scattering and inverse scattering by arbitrary anisotropic dielectric objects embedded in layered arbitrary anisotropic media," *IEEE Trans. Antennas Propag.*, vol. 68, no. 8, pp. 6473–6478, Aug. 2020.

[13] J. Li, J. Zhuo, Y. Chen, F. Han, and Q. H. Liu, "Retrieval of composite model parameters for 3-D microwave imaging of biaxial objects by BCGS-FFT and PSO," *IEEE Trans. Microw. Theory Techn.*, vol. 68, no. 5, pp. 1896–1907, May 2020.

[14] J. Li, J. Zhuo, Z. Guan, F. Han, and Q. H. Liu, "3-D electromagnetic scattering and inverse scattering by magnetodielectric objects with arbitrary anisotropy in layered uniaxial media," *IEEE Trans. Antennas Propag.*, vol. 68, no. 2, pp. 1009–1022, Feb. 2020.

[15] J. Zhuo, L. Ye, F. Han, L. Xiong, and Q. H. Liu, "Multiparametric electromagnetic inversion of 3-D biaxial anisotropic objects embedded in layered uniaxial media using VBIM enhanced by structural consistency constraint," *IEEE Trans. Antennas Propag.*, vol. 68, no. 6, pp. 4774–4785, Jun. 2020.

[16] Z. Wang, A. C. Bovik, H. R. Sheikh, and E. P. Simoncelli, "Image quality assessment: From error visibility to structural similarity," *IEEE Trans. Image Process.*, vol. 13, no. 4, pp. 600–612, Apr. 2004.